



This is a repository copy of *Performance of QCT-Derived scapula finite element models in predicting local displacements using digital volume correlation*.

White Rose Research Online URL for this paper:  
<http://eprints.whiterose.ac.uk/147233/>

Version: Accepted Version

---

**Article:**

Kusins, J., Knowles, N., Ryan, M. et al. (2 more authors) (2019) Performance of QCT-Derived scapula finite element models in predicting local displacements using digital volume correlation. *Journal of the Mechanical Behavior of Biomedical Materials*, 97. pp. 339-345. ISSN 1751-6161

<https://doi.org/10.1016/j.jmbbm.2019.05.021>

---

Article available under the terms of the CC-BY-NC-ND licence  
(<https://creativecommons.org/licenses/by-nc-nd/4.0/>).

**Reuse**

This article is distributed under the terms of the Creative Commons Attribution-NonCommercial-NoDerivs (CC BY-NC-ND) licence. This licence only allows you to download this work and share it with others as long as you credit the authors, but you can't change the article in any way or use it commercially. More information and the full terms of the licence here: <https://creativecommons.org/licenses/>

**Takedown**

If you consider content in White Rose Research Online to be in breach of UK law, please notify us by emailing [eprints@whiterose.ac.uk](mailto:eprints@whiterose.ac.uk) including the URL of the record and the reason for the withdrawal request.



[eprints@whiterose.ac.uk](mailto:eprints@whiterose.ac.uk)  
<https://eprints.whiterose.ac.uk/>

1  
2  
3  
4  
5  
6  
7  
8  
9  
10  
11  
12  
13  
14  
15  
16  
17  
18  
19  
20  
21  
22  
23  
24  
25  
26  
27  
28  
29  
30

# Performance of QCT-Derived Scapula Finite Element Models in Predicting Local Displacements Using Digital Volume Correlation

Jonathan Kusins<sup>1,2</sup>, Nikolas Knowles<sup>1,2</sup>, Melissa Ryan<sup>3,4</sup>, Enrico Dall'Ara<sup>3,4</sup>, Louis Ferreira<sup>1,2,\*</sup>

<sup>1</sup>Department of Mechanical and Materials Engineering  
Western University  
London, Canada

<sup>2</sup>Roth|McFarlane Hand and Upper Limb Centre  
St. Joseph's Health Care  
London, Canada

<sup>3</sup>Department of Oncology and Metabolism  
University of Sheffield  
Sheffield, United Kingdom

<sup>4</sup>Insigneo Institute for In Silico Medicine  
University of Sheffield  
Sheffield, United Kingdom

**\*Correspondence Address:**

Louis M. Ferreira, PhD  
Roth|McFarlane Hand and Upper Limb Centre,  
Surgical Mechatronics Laboratory, St. Josephs Health Care,  
268 Grosvenor St. London, ON, Canada.  
Tel: +1 519 646 6000 X. 61351  
E-mail address: Louis.Ferreira@sjhc.london.on.ca

**Keywords:** Subject-specific finite element analysis; digital volume correlation; shoulder FEM; CT-compatible loading.

33 **Abstract**

34           Subject-specific finite element models (FEMs) of the shoulder complex are commonly  
35 used to predict differences in internal load distribution due to injury, treatment or disease.  
36 However, these models rely on various underlying assumptions, and although experimental  
37 validation is warranted, it is difficult to obtain and often not performed. The goal of the current  
38 study was to quantify the accuracy of local displacements predicted by subject-specific QCT-based  
39 FEMs of the scapula, compared to experimental measurements obtained by combining digital  
40 volume correlation (DVC) and mechanical loading of cadaveric specimens within a microCT  
41 scanner.

42           Four cadaveric specimens were loaded within a microCT scanner using a custom-designed  
43 six degree-of-freedom hexapod robot augmented with carbon fiber struts for radiolucency.  
44 BoneDVC software was used to quantify full-field experimental displacements between pre- and  
45 post-loaded scans. Corresponding scapula QCT-FEMs were generated and three types of boundary  
46 conditions (BC) (idealized-displacement, idealized-force, and DVC-derived) were simulated for  
47 each specimen.

48           DVC-derived BCs resulted in the closest match to the experimental results for all  
49 specimens (best agreement: slope ranging from 0.87 - 1.09; highest correlation:  $r^2$  ranging from  
50 0.79-1.00). In addition, a two orders of magnitude decrease was observed in root-mean-square  
51 error when using QCT-FEMs with simulated DVC-derived BCs compared to idealized-  
52 displacement and idealized-force BCs.

53           The results of this study demonstrate that scapula QCT-FEMs can accurately predict local  
54 experimental full-field displacements if the BCs are derived from DVC measurements.

## 55 **1. Introduction**

56 Subject-specific finite element models (FEMs) of the shoulder complex provide the capability to  
57 predict the internal load distribution of the joint. Although quantitative computed tomography  
58 (QCT)-derived FEMs have been accepted as an established research tool to further understand the  
59 mechanics of the shoulder (Allred et al., 2016; Terrier et al., 2005; Zheng et al., 2017), the accuracy  
60 of predictions generated by these models is to some extent unknown. Currently, experimental  
61 validation of QCT-FEMs of the shoulder is limited to localized predictions of strain on the cortical  
62 shell (Dahan et al., 2016; Gupta et al., 2004); while the accuracy of internal predictions within the  
63 trabecular bone has yet to be explored.

64 To observe the internal load distribution within human bone, recent experimental protocols  
65 have combined mechanical loading with simultaneous time-lapsed volumetric imaging of bone  
66 specimens undergoing deformation (Nazarian and Müller, 2004). Digital volume correlation  
67 (DVC) techniques have been introduced to quantify full-field localized displacement  
68 measurements between pre- and post-loaded volumetric images (Grassi and Isaksson, 2015;  
69 Roberts et al., 2014). In addition, previous experimental studies that have combined volumetric  
70 imaging with DVC analysis techniques have shown great promise to elucidate internal fracture  
71 mechanisms by quantifying progressive strain and damage evolution within composite materials  
72 (Croom et al., 2016, 2019, 2017). To acquire volumetric images of a deformed specimen, a CT-  
73 compatible loading device is required. Current CT-compatible joint loading devices are based on  
74 screw-type mechanisms and are restricted by the degrees-of-freedom (dof) of load they can apply  
75 (Du et al., 2015; Jackman et al., 2016; Martelli and Perilli, 2018; Palanca et al., 2016; Sukjamsri  
76 et al., 2015; Zhou et al., 2018). However, to properly replicate physiological joint loads at the  
77 shoulder complex, a 6-dof loading mechanism would be desirable. Regardless, current

78 experimental protocols developed with DVC techniques have shown tremendous promise by  
79 quantifying internal localized deformations within trabecular bone that otherwise cannot be  
80 captured experimentally (Bay et al., 1999; Chen et al., 2017; Gillard et al., 2014; Liu and Morgan,  
81 2007).

82 DVC has been applied at the micro (e.g. trabecular bone cores) and joint level (e.g.  
83 vertebra) to validate  $\mu$ CT- and QCT-FEMs respectively (Chen et al., 2017; Costa et al., 2017;  
84 Hussein et al., 2018; Jackman et al., 2016; Mao et al., 2019, p.; Zauel et al., 2005). At the micro  
85 level, the accuracy of the predictions generated by  $\mu$ CT-FEMs was found to be sensitive to the  
86 boundary condition (BC) modelled (Chen et al., 2017). Specifically, when using BCs derived  
87 directly from local DVC measurements, any inherent experimental limitations (e.g. specimen  
88 fixation rigidity or structural stiffness of the loading mechanism) were assumed to be eliminated  
89 and thus excellent agreement (slope ( $m$ )  $\approx 1$ , coefficient of determination ( $r^2$ )  $\approx 1$ , y-intercept ( $b$ )  
90  $\approx 0$ ) was achieved (Chen et al., 2017; Costa et al., 2017; Oliviero et al., 2018). However, when  
91 extrapolating these techniques to QCT-FEMs at the joint level, similar success has not been  
92 reported. Previous studies performed by Jackman et. al. and Hussein et. al. within the vertebra  
93 found improvements in performance of QCT-FEMs when using BCs derived from DVC  
94 measurements obtained at the yield point; but only moderate agreement between the experimental  
95 local displacements and FEM predictions were observed (Hussein et al., 2018; Jackman et al.,  
96 2016). A similar validation study has yet to be performed to quantify the performance of shoulder  
97 QCT-FEMs in predicting local experimental displacement measurements obtained through DVC.

98 Hence, the primary objective of the current study was to quantify the accuracy of local  
99 displacements predicted by subject-specific shoulder QCT-FEMs compared to experimental  
100 measurements obtained through mechanical loading and simultaneous volumetric imaging of

101 cadaveric scapular specimens. A secondary objective was the design and fabrication of a CT-  
102 compatible 6-dof loading apparatus capable of applying articular loads within a microCT scanner.

## 103 **2. Materials and Methods**

### 104 **2.1 Development of a CT-Compatible 6-DOF Loading Apparatus**

105 A custom 6-dof hexapod parallel robot was designed to apply external loads to a scapula. The  
106 robot consisted of a base, loading platform and six prismatic actuators that connected the base and  
107 platform (Figure 1) in a configuration consistent with a Stewart platform design. Although  
108 variations exist, the Stewart platform design commonly uses six linear actuators attached in pairs  
109 by universal joints to a movable platform and fixed base. Each prismatic actuator is composed of  
110 a lead screw mechanism driven by independent servo-motors. Although the robot consisted of only  
111 linear actuators, its hexapod configuration transforms linear displacements into complete 6-dof  
112 motions that include all possible translations and rotations, within its range of motion. In addition,  
113 the Stewart platform design is noted to have a high load carrying capacity within a small working  
114 envelope and has been used in previous applications involving 6-dof biomechanical testing  
115 applications (Boyin Ding et al., 2011; Lawless et al., 2014; Walker and Dickey, 2007).

116 The hexapod robot was augmented with radiolucent carbon fiber extensions to provide CT-  
117 compatibility with a Nikon XT H 225ST cone-beam microCT scanner. Custom fixtures were  
118 fabricated to allow for loads to be applied to the glenoid of a cadaveric scapula within a microCT  
119 scanner. A hemispherical platen (diameter equal to 48 mm) was fabricated from acetal plastic and  
120 attached to the loading platform via an acrylic extension rod. A 6-dof load cell (Mini 45, ATI  
121 Industrial Automation, NC, USA) was instrumented to the loading platform to provide real-time

122 force feedback during the experimental loading protocol. Overall, the current system can apply 1.5  
123 kN of compression and weighs 9.6 kg.

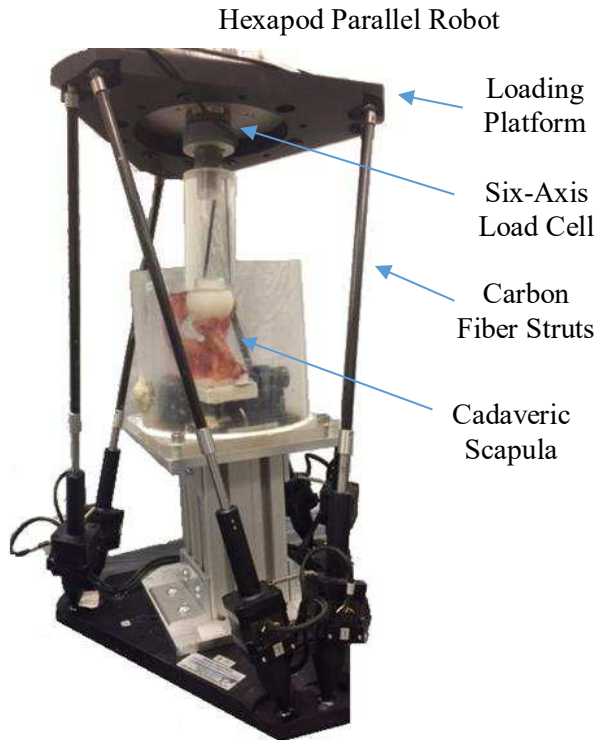


**Figure 1:** A custom-designed six degree-of-freedom hexapod robot was used to experimentally load cadaveric scapulae within a cone-beam microCT scanner. The use of carbon fiber struts provided radiolucent sections to reduce any imaging artifacts that may occur with use of the hexapod robot.

124

## 125 **2.2 Specimen Preparation and Experimental Loading**

126 Four cadaveric shoulders (two male and two female) were tested (Table 1). Prior to experimental  
127 loading, the specimens with soft tissue intact were imaged within a clinical QCT-scanner (GE  
128 Discovery CT750 HD, Milwaukee, WI, USA) at clinical scan settings (pixel size: 0.625 mm to  
129 0.668 mm, slice thickness: 0.625 mm, 120 kVp, 200 mA, BONEPLUS). A dipotassium phosphate  
130 ( $K_2HPO_4$ ) calibration phantom (QCT Pro, Mindways Software Inc., Austin, TX, USA) was  
131 included in each QCT scan for specimen-specific QCT-density relationships. QCT scans obtained

132 at clinical resolution were used for development of continuum-level QCT-derived finite element  
 133 models described further in Section 2.4. Following the scanning protocol, each scapula was  
 134 denuded of all soft tissue. The glenoid articular surface was resurfaced using a clinical shoulder  
 135 reaming tool to provide a consistent uniform surface for experimental loading. The scapula was  
 136 then cut on a medial plane (sectioned approximately 55 mm from the articular surface) and  
 137 cemented in polymethyl methacrylate (PMMA) for fixation in the hexapod robot. A custom jig  
 138 was used to orient the axis at which the glenoid was resurfaced perpendicular to the loading  
 139 platform of the hexapod robot.

140 Table 1: Age, sex, and QCT density ( $\pm 1$  SD) of cadaveric scapulae specimens.

	Sex	Age	QCT Density ( $\text{g}_{\text{K}_2\text{HPO}_4}/\text{cm}^3$ )
Specimen 1	Male	80	$0.333 \pm 0.256$
Specimen 2	Male	73	$0.245 \pm 0.198$
Specimen 3	Female	62	$0.376 \pm 0.240$
Specimen 4	Female	52	$0.377 \pm 0.253$

141 Experimental loading for each scapula was performed within a cone-beam microCT  
 142 scanner (Nikon XT H 225ST). Each specimen was wrapped with tissue-soaked phosphate-buffered  
 143 saline solution to ensure hydration throughout the scanning protocol. The hexapod robot,  
 144 previously described, was used to apply external loads. Consistent for each specimen, an initial  
 145 stabilizing load (10 N, settling time of 20 minutes to allow for specimen relaxation) was applied  
 146 and a pre-loaded microCT scan was acquired (33.5  $\mu\text{m}$  isotropic voxel size, 95 kVp, 64  $\mu\text{A}$ , 3141  
 147 projections, 55 minute scan time, 1000 ms exposure). Two post-loaded scans of the specimen were  
 148 then obtained with identical settings as the pre-loaded scan. The first load consisted of a target  
 149 compressive load of 500 N with a settling time of 20 minutes. The second load consisted of a target  
 150 500 N load applied off-axis,  $5^\circ$  posterior for each specimen and  $5^\circ$  inferior for specimens 1, 2, and  
 151 4 with respect to the robot's frame. An inferior off-axis angle was not applied to specimen 3 due

152 to interference between the acrylic extension rod and the acromion of the specimen. Both loading  
153 cases were performed directly within the microCT scanner, without repositioning the loading  
154 apparatus between scans. Load cell measurements were acquired via a NI-USB 6210 data  
155 acquisition unit (National Instruments Corporation, Austin, Texas) obtained after the 20 minutes  
156 settling time but prior to the microCT scan. The resulting field of view (FOV) for each scan was a  
157 cube with edge lengths of 65 mm, which captured the glenoid vault (approximately 25 mm medial  
158 from the articular surface) and the loading platen in the pre- and post-loaded states.

### 159 **2.3 Digital Volume Correlation**

160 Local experimental displacement measurements between the pre- and post-loaded images were  
161 obtained using DVC algorithms (Figure 2). To prepare the images for DVC, a specimen-specific  
162 threshold was applied (Mimics v.20.0, Materialise, Leuven, BE) to segment and isolate the glenoid  
163 vault from other objects captured within the microCT scans (e.g. loading platen). Values outside  
164 the selected threshold were assigned a constant grey level value similar to bone marrow (equivalent  
165 to 85 in 8-bit greyscale). The images were then cropped and converted to 8-bit greyscale (ImageJ,  
166 NIH) (Schneider et al., 2012).

167 A previously established and validated deformable image registration toolkit, BoneDVC,  
168 was used to quantify the full-field experimental displacement field between the pre- and post-  
169 loaded images (Dall'Ara et al., 2017, 2014). BoneDVC is a global based DVC approach that  
170 computes full-field local displacement vectors between two sets of volumetric images using cross  
171 correlation techniques (Dall'Ara et al., 2014). Furthermore, BoneDVC has previously been used  
172 to validate  $\mu$ FEMs for various osseous structures (Chen et al., 2017; Costa et al., 2017; Oliviero et  
173 al., 2018). To compute the precision of the local displacement measurements quantified by

174 BoneDVC, a standard procedure of comparing two pre-loaded scans with various nodal spacing  
 175 was performed (Dall’Ara et al., 2017, 2014). Based on these results, a nodal spacing of 30 voxels,  
 176 (approximately 1 mm), was decided as an optimal tradeoff between spatial resolution and precision  
 177 (error along x, y, and z direction lower than 2.5  $\mu\text{m}$ ).

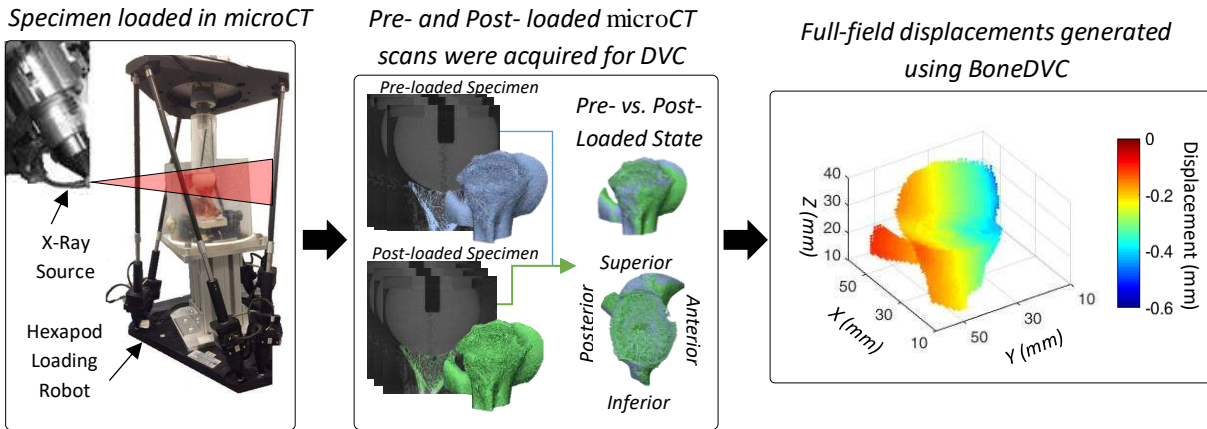


**Figure 2:** Four scapula specimens were scanned within a microCT at a resolution of 33.5  $\mu\text{m}$  in pre- and post-loaded states. Full-field local displacements (sub-volume size  $\approx 1$  mm) between the pre- and post-loaded scans were obtained using BoneDVC.

178

179 **2.4 Computational In-Silico Modelling**

180 Specimen-specific QCT-FEMs were generated for each scapula to simulate the experimental  
 181 loading set-up. The geometry of each scapula was extracted from the corresponding QCT scan  
 182 acquired prior to experimental loading. To identify the medial border at which the experimental  
 183 scapulae were cut, laser surface scans (Artec Spider, Artec 3D, Luxembourg) were acquired for  
 184 each prepared specimen. From these, STL models were generated and registered to the QCT  
 185 models. Anything below the PMMA surface was removed by Boolean subtraction. In addition,  
 186 any elements within the volume of the reamed articular surface were removed to match the  
 187 prepared cadaveric scapulae. A surface triangular mesh was generated (3-matic v.12.0,  
 188 Materialise, Leuven, BE) with a target edge length of 1 mm (Burkhart et al., 2013). The surface

189 mesh was then converted to a quadratic tetrahedral mesh using ABAQUS (v.6.14, Simulia,  
190 Providence, RI). Linear elastic isotropic material properties were applied to the volumetric mesh  
191 (Mimics v.20.0, Materialise, Leuven, BE) based on the local density measure using Eq.1 and Eq.  
192 2 (Rice et al., 1988; Schaffler and Burr, 1988).

$$\rho_{app} < 1.54 \text{ g/cm}^3 \quad E_{trab} = 60 + 900 * \rho_{app}^2 \quad (\text{Eq. 1})$$

$$\rho_{app} \geq 1.54 \text{ g/cm}^3 \quad E_{cort} = 90 * \rho_{app}^{7.4} \quad (\text{Eq. 2})$$

193 Where  $E_{trab}$  is Young's modulus of trabecular bone [MPa],  $E_{cort}$  is Young's modulus of cortical  
194 bone [MPa], and  $\rho_{app}$  is apparent density.

195 To register the QCT-FEMs to the coordinate system of the microCT, an iterative closest points  
196 algorithm (3-matic Research 11.0, Materialise, Leuven, BE) was performed aligning the outer  
197 geometry of the QCT-derived scapula to the corresponding microCT-derived scapula (Knowles et  
198 al., 2019).

199 Three separate boundary conditions (BCs) were modelled (ABAQUS v.6.14, Simulia,  
200 Providence, RI) to investigate their effect on the accuracy of the QCT-FEMs. The first two  
201 simulations consisted of idealized BCs (idealized-displacement BC and idealized-force BC). For  
202 both idealized BCs, a deformable virtual loading platen, meshed with hexahedral elements ( $E =$   
203  $3100 \text{ MPa}$ ,  $\nu = 0.35$ ), was constructed and general contact between the virtual platen and scapula  
204 was modelled (coefficient of friction = 0.2). The medial border of the scapula was assumed to be  
205 fixed and either a force (idealized-force BC) or displacement (idealized-displacement BC) was  
206 applied to the virtual loading platen (Figure 3). For the idealized-force BC, the experimental force  
207 measured immediately prior to the microCT scan was prescribed to the top nodes of the virtual  
208 loading platen. For the idealized-displacement BC, a displacement was prescribed to the top nodes  
209 of virtual loading platen forcing the platen to the post-loaded experimental position. The

210 experimental post-loaded position of the loading platen was quantified by segmenting out the  
211 experimental platen in the corresponding raw post-loaded microCT image.

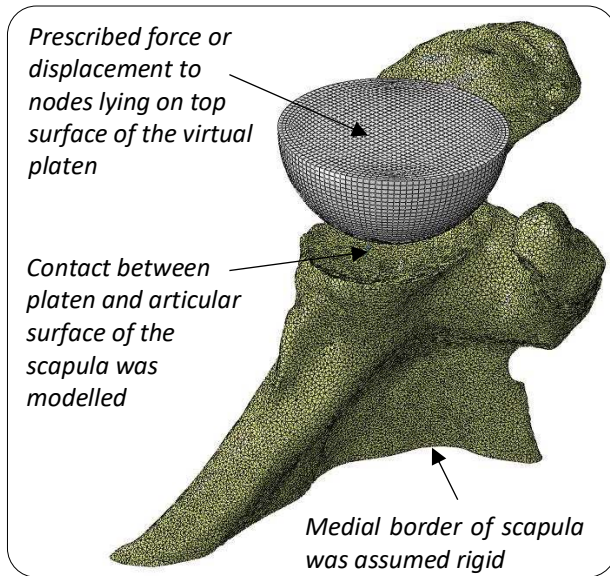


**Figure 3:** Specimen-specific QCT-FEMs with idealized BCs were modelled. Idealized BCs assumed the medial border of the scapula was fixed and either a displacement (idealized-displacement) or force (idealized-force) was applied to the virtual loading platen.

212

213 In addition, DVC-derived BCs were modelled (Chen et al., 2017; Costa et al., 2017;  
214 Jackman et al., 2016; Zuel et al., 2005) (Figure 4). First, to generate the DVC-derived BCs, each  
215 specimen was further cropped medially due to the limited FOV of the microCT scans.  
216 Subsequently, local displacements were prescribed to each node lying on the articular surface of  
217 the glenoid and the medial surface of the cropped scapula. A custom Matlab code (v.R2017a,  
218 Mathworks, Natick, MA) applied tri-linear interpolation to local displacements provided by the  
219 DVC measurements onto the corresponding QCT-FEM nodes.

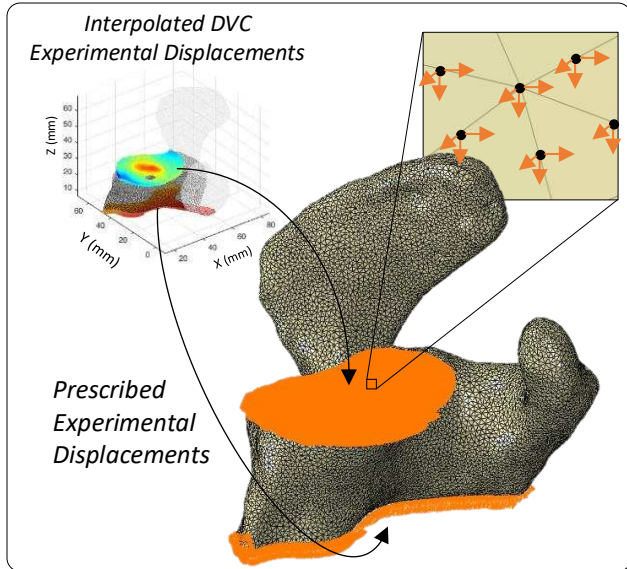


**Figure 4:** DVC-derived BCs were modelled by assigning local experimental displacements obtained by DVC directly to the articular and medial surface of the QCT-FEM scapula.

220

## 221 2.5 Statistical Analysis

222 To quantify the performance of the scapula QCT-FEMs, local displacement predictions were  
 223 compared to DVC experimental measurements using linear regression. To pair the outcome  
 224 measures, local DVC displacements were paired with averaged QCT-FEM predicted  
 225 displacements, region averaged within a 1mm cubic voxel, equivalent to the DVC nodal spacing  
 226 and dependent on the nodal location of the DVC measurement (Hussein et al., 2018; Jackman et  
 227 al., 2016). Furthermore, to exclude any measurements prescribed by the DVC-derived BCs, only  
 228 nodes within the middle 80% of the scanned specimen were used for comparison. Outliers were  
 229 removed from the paired QCT-FEM predictions and local DVC results along the x, y, and z  
 230 direction using 5x the Cook's distance (Costa et al., 2017). Slope (m), coefficient of determination  
 231 ( $r^2$ ) and root-mean-square error (RMSE) were quantified for both loading conditions (compressive  
 232 and off-axis) and with each BC (idealized-force, idealized-displacement, and DVC-derived).

233 In addition, reaction forces predicted by the QCT-FEMs with idealized-displacement BCs  
234 and DVC-derived BCs were compared to the experimental applied force. Idealized-force BCs was  
235 not included, as the input force required to generate the model was equal to the experimentally  
236 measured force. Absolute percentage error was quantified for each specimen and for both loading  
237 cases.

### 238 **3. Results**

239 The accuracy of predictions generated by the QCT-FEMs was found to be highly sensitive to the  
240 boundary conditions simulated. For all four specimens subjected to the compressive load, the  
241 performance of QCT-FEMs in predicting experimental local displacements were vastly improved  
242 with DVC-derived BCs (Table 2, Figure 5). DVC-derived BCs resulted in the closest match to the  
243 experimental results, with ranges of  $m = 0.93 - 1.05$ ,  $b = -0.02 - 0.01$ , and  $r^2 = 0.83 - 1.00$  for each  
244 specimen along the x, y, and z direction. Similar agreement between the experimental and QCT-  
245 FEM predictions were not obtained when using idealized BCs. High variations within  $m$  ( $-0.13 -$   
246  $1.66$ ),  $b$  ( $-0.09 - 0.28$ ) and  $r^2$  ( $0.002 - 0.93$ ) were observed for QCT-FEMs with idealized-force  
247 BCs. In addition, high variations in  $m$  ( $-0.03 - 2.84$ ),  $b$  ( $-0.29 - 0.75$ ), and  $r^2$  ( $0.001 - 0.95$ ) were  
248 observed when using idealized-displacement BCs for all specimens. Overall, RMSE was decreased  
249 by two orders of magnitude when using DVC-derived BCs (average RMSE of  $4.1 \pm 0.9 \mu\text{m}$ ,  $4.7 \pm 2.2 -$   
250  $\mu\text{m}$ ,  $4.8 \pm 2.3 \mu\text{m}$  along x, y, and z direction respectively) compared to the idealized-force BC  
251 (average RMSE of  $414 \pm 479 \mu\text{m}$ ,  $401 \pm 356 \mu\text{m}$ ,  $331 \pm 170 \mu\text{m}$  along x, y, and z direction  
252 respectively) and idealized-displacement BC (average RMSE of  $367 \pm 342 \mu\text{m}$ ,  $322 \pm 273 \mu\text{m}$ ,  
253  $175 \pm 96 \mu\text{m}$  along x, y, and z direction respectively).

254 Table 2: Linear regression results between local displacements predicted by QCT-based FEMs and  
 255 DVC experimental results due to a compressive load.

Specimen #		Slope (m)			y-intercept (b)			Coefficient of Correlation ( $r^2$ )			Root Mean Square Error (RMSE) ( $\mu\text{m}$ )		
		x	y	z	x	y	z	x	y	z	x	y	z
Idealized-Force BC	1	0.52	0.21	0.11	0.12	0.08	0.00	0.89	0.38	0.10	237	447	234
	2	-0.02	-0.10	-0.13	0.00	0.07	-0.09	0.01	0.59	0.47	37	866	565
	3	0.01	0.31	0.10	0.02	-0.07	-0.02	< 0.01	0.50	0.48	1117	274	248
	4	1.05	1.66	0.88	0.28	-0.01	0.17	0.93	0.82	0.77	265	18	199
Idealized-Displacement BC	1	2.84	1.00	0.54	0.66	0.39	-0.02	0.95	0.37	0.06	211	398	158
	2	-0.03	0.17	0.08	-0.11	0.05	-0.29	< 0.01	0.01	< 0.01	126	655	299
	3	0.90	0.96	1.01	0.75	-0.20	0.06	0.48	0.16	0.94	873	223	66
	4	1.39	1.69	1.65	0.38	0.00	0.31	0.85	0.62	0.82	258	12	178
DVC-Derived BC	1	1.00	0.99	1.01	0.00	-0.01	0.00	0.97	0.98	0.99	4.9	6.7	6.4
	2	0.99	0.99	1.00	0.00	0.01	0.00	0.99	1.00	1.00	2.9	2.5	2.5
	3	0.99	1.05	1.02	-0.01	-0.02	0.00	1.00	0.95	1.00	4.7	6.5	7.3
	4	0.93	0.93	1.02	-0.02	0.00	0.00	0.97	0.83	0.99	3.6	3.1	3.2

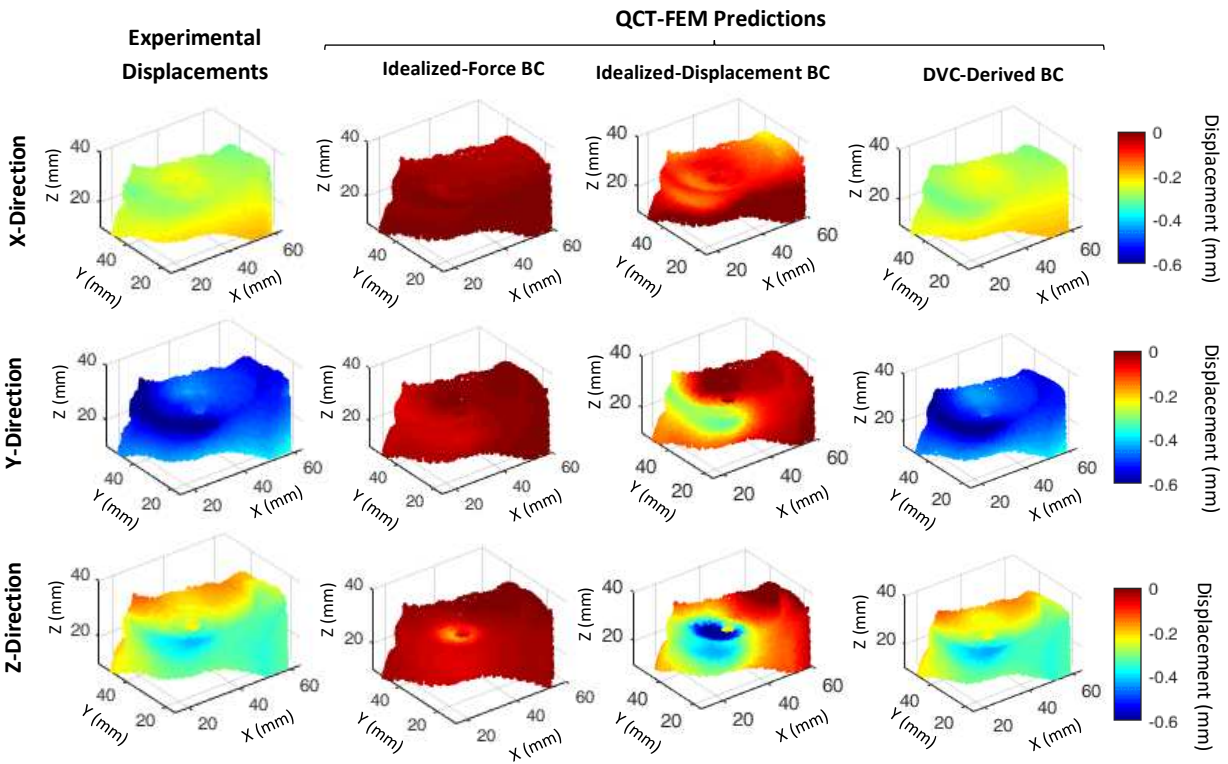


Figure 5: Representative full-field experimental displacements for specimen 1 during a compressive load, compared to predictions generated by a QCT-FEM with idealized-force BC, idealized-displacement BC, and DVC-derived BC.

257 For the off-axis load, similar results to the compressive load were observed (Table 3). High  
 258 variability in  $m$  (ranges  $-0.40 - 2.35$ ),  $b$  ( $-0.70 - 0.98$ ), and  $r^2$  ( $0.002 - 0.98$ ) were observed for both  
 259 idealized BCs. However, when using DVC-derived BCs, excellent agreement with the  
 260 experimental results were obtained with ranges of  $m$  ( $0.87 - 1.09$ ),  $b$  ( $-0.03 - 0.03$ ), and  $r^2$  ( $0.79 -$   
 261  $1.00$ ) for each specimen. In addition, RMSE between the QCT-FEM predictions and experimental  
 262 measurements was greatly reduced when using DVC-derived BCs (average RMSE of  $4.8 \pm 0.7 \mu\text{m}$ ,  
 263  $5.3 \pm 1.0 \mu\text{m}$ ,  $6.0 \pm 1.4 \mu\text{m}$  along  $x$ ,  $y$ , and  $z$  direction) compared to idealized-force BC (average  
 264 RMSE of  $541 \pm 268 \mu\text{m}$ ,  $443 \pm 681 \mu\text{m}$ ,  $337 \pm 225 \mu\text{m}$  along  $x$ ,  $y$ , and  $z$  direction) and idealized-  
 265 displacement BC (average RMSE of  $494 \pm 343 \mu\text{m}$ ,  $345 \pm 484 \mu\text{m}$ ,  $196 \pm 147 \mu\text{m}$  along the  $x$ ,  $y$ , and  
 266  $z$  direction).

267 Table 3: Linear regression results between local displacements predicted by QCT-based FEMs and  
 268 DVC experimental results due to an off-axis load.

Specimen #	Slope ( $m$ )			y-intercept ( $b$ )			Coefficient of Correlation ( $r^2$ )			Root Mean Square Error (RMSE) ( $\mu\text{m}$ )			
	$x$	$y$	$z$	$x$	$y$	$z$	$x$	$y$	$z$	$x$	$y$	$z$	
Idealized-Force BC	1	-0.04	-0.40	0.53	-0.01	0.14	0.09	< 0.01	0.08	0.74	311	110	185
	2	-0.07	-0.02	-0.05	-0.03	0.03	-0.05	0.55	0.14	0.31	719	1460	670
	3	0.79	0.90	0.80	0.57	-0.15	0.20	0.98	0.92	0.98	822	175	260
	4	0.68	1.20	0.61	0.20	-0.03	0.13	0.89	0.68	0.66	311	28	230
Idealized-Displacement BC	1	0.47	0.32	1.53	0.16	0.09	0.24	0.09	0.02	0.84	322	66	139
	2	0.86	0.75	0.78	0.29	-0.70	0.25	0.75	0.80	0.74	394	1063	405
	3	0.99	0.89	1.18	0.98	-0.19	0.06	0.43	0.07	0.93	1001	233	62
	4	2.13	2.35	2.27	0.64	-0.03	0.48	0.84	0.60	0.79	259	35	177
DVC-Derived BC	1	1.03	1.05	1.05	0.01	-0.01	0.01	0.96	0.98	0.99	4.2	4.4	6.6
	2	0.98	0.98	1.00	-0.02	0.03	0.00	0.99	1.00	1.00	5.8	5.0	5.0
	3	0.99	1.09	1.01	-0.01	-0.03	0.00	1.00	0.95	1.00	4.9	6.7	7.8
	4	1.03	0.87	1.00	0.01	0.00	0.00	0.97	0.79	0.98	4.2	5.1	4.8

269 High percentage errors (average error = 333%, range = 169 - 429%) in reaction forces were  
 270 required to displace the virtual loading platen when using idealized-displacement BCs.  
 271 Comparatively, the percentage error was reduced when using QCT-FEMs with DVC-derived BCs  
 272 (average error = 32%, range = 8 - 44%). Similar results were observed with an off-axis load, with

273 higher percentage errors when using idealized-displacement BCs (average error = 350%, range =  
274 152 - 520%) compared to DVC-derived BCs (average error = 26%, range = 6 - 50%).

#### 275 **4. Discussion**

276 The goal of the current study was to quantify the performance of scapula QCT-FEMs in predicting  
277 local displacement measurements obtained from combining digital volume correlation (DVC) and  
278 mechanical loading within a microCT scanner. Due to the inability to resolve trabecular  
279 microarchitecture at a resolution associated with clinical in-vivo imaging of bone, QCT-FEMs rely  
280 on continuum-level assumptions and ignore the geometry of the inner trabecular network.  
281 However, the accuracy of local predictions generated by subject-specific vertebra QCT-FEMs has  
282 recently been questioned (Hussein et al., 2018; Jackman et al., 2016). The results of the current  
283 study found that QCT-FEMs of the scapula can accurately predict local displacement  
284 measurements when using DVC-derived BCs. A two orders of magnitude decrease was observed  
285 in RMSE, when using QCT-FEMs with simulated DVC-derived BCs compared to the idealized  
286 BCs during a compressive or off-axis load. Furthermore, excellent agreement ( $m$  ranging from  
287 0.87 - 1.09,  $r^2$  ranging from 0.79 - 1.00) was found between experimental results and QCT-FEM  
288 predictions when using DVC-derived BCs, consistent with previous studies performed using  $\mu$ -  
289 FEMs on different bone structures (Chen et al., 2017; Costa et al., 2017; Oliviero et al., 2018).  
290 Reaction forces predicted by the QCT-FEMs with DVC-derived BCs were also within reasonable  
291 error (compressive error range 8 - 44%, off-axis error range 6 - 50%). The excellent performance  
292 of the QCT-FEMs with DVC-derived BCs within the current study may partly be attributed to the  
293 fact that loading only within the elastic range was performed, simplifying the QCT-FEMs  
294 generated, compared to step-wise fracture loading previously performed (Hussein et al., 2018;  
295 Jackman et al., 2016). In addition, inherent differences between the vertebra and scapula, and their

296 constitutive equations used to assign material properties may contribute to the performance  
297 differences in QCT-FEMs of this study compared to previous vertebral studies. Therefore,  
298 although excellent agreement between the QCT-FEM predictions and DVC results were observed  
299 within the current study in the shoulder, it is unknown whether these findings can be extrapolated  
300 to QCT-based FEMs of other joints.

301 To perform cadaveric experimental loading within a microCT, a secondary objective  
302 included the design of a CT-compatible loading device. The robot's ability to generate articular  
303 loads within a small working envelope overcame a major design constraint imposed by space  
304 restrictions within a CT scanner. Furthermore, controlled loading in 6-dof is a marked  
305 improvement over previously developed screw-based CT-compatible devices (Jackman et al.,  
306 2016; Martelli and Perilli, 2018; Palanca et al., 2016; Sukjamsri et al., 2015). Precision of the DVC  
307 measurements was found not to be affected by the hexapod robot, as errors  $< 2.5 \mu\text{m}$  along each  
308 Cartesian direction were recorded during the repeated scans procedure further demonstrating the  
309 feasibility of the apparatus.

310 For QCT-FEMs with idealized-force BCs, local displacement predictions generally  
311 underestimated the experimental results. In addition, computed reaction forces required to displace  
312 the virtual platen were much higher in QCT-FEMs with idealized-displacement BCs compared to  
313 idealized-force BCs. This may suggest that the QCT-FEMs may have been too stiff due to over-  
314 constrained idealized BCs. Only stiffness of the specimen mount (including the PMMA cement)  
315 is relevant, since the experimental displacement was measured from microCT rather than from the  
316 apparatus itself. Potentially, local DVC displacement measurements could have been applied to  
317 the bottom surface of the idealized QCT-FEMs and this may have reduced the observed  
318 differences; however, this would require localized displacement measures as an input into the

319 QCT-FEMs that may not always be attainable. Nonetheless, stiffness of the experimental setup  
320 was not accounted for in this study, as the idealized BCs were modelled according to the literature  
321 (Chen et al., 2017; Jackman et al., 2016). Now that it has been observed that QCT-FEMs with  
322 DVC-derived BCs can in fact replicate experimental displacement measures, future work could  
323 include modelling the experimental apparatus to allow for the QCT-FEMs to become more  
324 generalizable.

325         Limitations within the current study should be noted. First, QCT-FEMs were only validated  
326 using linear-isotropic material properties subjected to elastic loads. Therefore, further validation  
327 is required to investigate failure mechanisms that arise due to loading within the inelastic region.  
328 Furthermore, only local displacement measurements and global reaction forces were used to  
329 quantify the performance of scapula QCT-FEMs. While strain is a commonly used metric  
330 produced by QCT-FEMs to predict failure, experimental strains calculated from microCT-based  
331 DVC displacements exhibit higher uncertainties. As the scope of the current study only included  
332 evaluating local displacements and global reaction forces, the impact of boundary conditions on  
333 other local outcome predictions such as strain was not explored. A Synchrotron light source could  
334 be used which may reduce experimental uncertainties (Comini et al., 2019; Palanca et al., 2017);  
335 however, this was outside the scope of the current study. Finally, the low sample size ( $n = 4$ ) of  
336 this study is a limitation, which was a product of the complex and time-consuming loading and  
337 imaging protocol.

338         The results of the study demonstrate that errors in local displacements predicted by QCT-  
339 FEMs of the shoulder can be minimized using DVC-derived boundary conditions. This work also  
340 demonstrated that a novel CT-compatible hexapod robot design was effective for applying 6-dof  
341 loading vectors to a scapula while acquiring high-resolution microCT scans in a cone beam

342 scanner. Combining volumetric imaging with DVC analysis allowed for the ability to evaluate  
343 full-field internal displacement predictions generated by the QCT-FEMs that otherwise could not  
344 be captured with traditional surface-based measurement techniques (Dahan et al., 2016; Lin et al.,  
345 2016). Further development of these methods should be conducted to examine fracture  
346 mechanisms.

## 347 **Acknowledgements**

348 The authors would like to thank Aoife Pucchio for her assistance with data collection. This research  
349 was supported by a Post Graduate Scholarship from the Natural Sciences and Engineering  
350 Research Council of Canada. Jonathan Kusins and Nikolas Knowles are supported in part by a  
351 Transdisciplinary Bone & Joint Training Award from the Collaborative Training Program in  
352 Musculoskeletal Health Research at Western University. Enrico Dall'Ara and Melissa Ryan were  
353 supported by the Engineering and Physical Sciences Research Council (Grant Number:  
354 EP/P015778/1).

## 355 **References**

- 356 Allred, J.J., Flores-Hernandez, C., Hoenecke Jr, H.R., D'Lima, D.D., 2016. Posterior augmented glenoid  
357 implants require less bone removal and generate lower stresses: a finite element analysis. *Journal*  
358 *of shoulder and elbow surgery* 25, 823–830. <https://doi.org/10.1016/j.jse.2015.10.003>
- 359 Bay, B.K., Smith, T.S., Fyhrie, D.P., Saad, M., 1999. Digital volume correlation: Three-dimensional  
360 strain mapping using X-ray tomography. *Exp. Mech.* 39, 217–226.  
361 <https://doi.org/10.1007/BF02323555>
- 362 Boyin Ding, Stanley, R.M., Cazzolato, B.S., Costi, J.J., 2011. Real-time FPGA control of a hexapod robot  
363 for 6-DOF biomechanical testing, in: *IECON 2011*. Presented at the *IECON 2011 - 37th Annual*  
364 *Conference of IEEE Industrial Electronics*, Melbourne, AU, pp. 252–257.  
365 <https://doi.org/10.1109/IECON.2011.6119320>
- 366 Burkhart, T.A., Andrews, D.M., Dunning, C.E., 2013. Finite element modeling mesh quality, energy  
367 balance and validation methods: A review with recommendations associated with the modeling of  
368 bone tissue. *J Biomech* 46, 1477–1488. <https://doi.org/10.1016/j.jbiomech.2013.03.022>
- 369 Chen, Y., Dall'Ara, E., Sales, E., Manda, K., Wallace, R., Pankaj, P., Viceconti, M., 2017. Micro-CT  
370 based finite element models of cancellous bone predict accurately displacement once the

371 boundary condition is well replicated: A validation study. *J Mech Behav Biomed Mater* 65, 644–  
372 651. <https://doi.org/10.1016/j.jmbbm.2016.09.014>

373 Comini, F., Palanca, M., Cristofolini, L., Dall'Ara, E., 2019. Uncertainties of synchrotron microCT-based  
374 digital volume correlation bone strain measurements under simulated deformation. *J Biomech* 86,  
375 232–237. <https://doi.org/10.1016/j.jbiomech.2019.01.041>

376 Costa, M.C., Tozzi, G., Cristofolini, L., Danesi, V., Viceconti, M., Dall'Ara, E., 2017. Micro Finite  
377 Element models of the vertebral body: Validation of local displacement predictions. *Plos One* 12,  
378 1–18. <https://doi.org/10.1371/journal.pone.0180151>

379 Croom, B., Wang, W.-M., Li, J., Li, X., 2016. Unveiling 3D Deformations in Polymer Composites by  
380 Coupled Micro X-Ray Computed Tomography and Volumetric Digital Image Correlation. *Exp.*  
381 *Mech.* 56, 999–1016. <https://doi.org/10.1007/s11340-016-0140-7>

382 Croom, B.P., Jin, H., Mills, B., Carroll, J., Long, K., Brown, J., Li, X., 2019. Damage mechanisms in  
383 elastomeric foam composites: Multiscale X-ray computed tomography and finite element  
384 analyses. *Compos Sci Technol* 169, 195–202. <https://doi.org/10.1016/j.compscitech.2018.11.025>

385 Croom, B.P., Xu, P., Lahoda, E.J., Deck, C.P., Li, X., 2017. Quantifying the three-dimensional damage  
386 and stress redistribution mechanisms of braided SiC/SiC composites by in situ volumetric digital  
387 image correlation. *Scr. Mater* 130, 238–241. <https://doi.org/10.1016/j.scriptamat.2016.12.021>

388 Dahan, G., Trabelsi, N., Safran, O., Yosibash, Z., 2016. Verified and validated finite element analyses of  
389 humeri. *J Biomech* 49, 1094–1102. <https://doi.org/10.1016/j.jbiomech.2016.02.036>

390 Dall'Ara, E., Barber, D., Viceconti, M., 2014. About the inevitable compromise between spatial  
391 resolution and accuracy of strain measurement for bone tissue: A 3D zero-strain study. *J Biomech*  
392 47, 2956–2963. <https://doi.org/10.1016/j.jbiomech.2014.07.019>

393 Dall'Ara, E., Peña-Fernández, M., Palanca, M., Giorgi, M., Cristofolini, L., Tozzi, G., 2017. Precision of  
394 Digital Volume Correlation Approaches for Strain Analysis in Bone Imaged with Micro-  
395 Computed Tomography at Different Dimensional Levels. *Front Mater Sci* 4, 1–13.  
396 <https://doi.org/10.3389/fmats.2017.00031>

397 Du, J., Lee, J.-H., Jang, A.T., Gu, A., Hossaini-Zadeh, M., Prevost, R., Curtis, D.A., Ho, S.P., 2015.  
398 Biomechanics and strain mapping in bone as related to immediately-loaded dental implants. *J*  
399 *Biomech* 48, 3486–3494. <https://doi.org/10.1016/j.jbiomech.2015.05.014>

400 Gillard, F., Boardman, R., Mavrogordato, M., Hollis, D., Sinclair, I., Pierron, F., Browne, M., 2014. The  
401 application of digital volume correlation (DVC) to study the microstructural behaviour of  
402 trabecular bone during compression. *J Mech Behav Biomed Mater* 29, 480–499.  
403 <https://doi.org/10.1016/j.jmbbm.2013.09.014>

404 Grassi, L., Isaksson, H., 2015. Extracting accurate strain measurements in bone mechanics: a critical  
405 review of current methods. *J Mech Behav Biomed Mater* 50, 43–54.  
406 <https://doi.org/10.1016/j.jmbbm.2015.06.006>

407 Gupta, S., Van Der Helm, F.C.T., Sterk, J.C., Van Keulen, F., Kaptein, B.L., 2004. Development and  
408 experimental validation of a three-dimensional finite element model of the human scapula. *Proc*  
409 *Inst Mech Eng H* 218, 127–142. <https://doi.org/10.1243/095441104322984022>

410 Hussein, A.I., Louzeiro, D.T., Unnikrishnan, G.U., Morgan, E.F., 2018. Differences in Trabecular  
411 Microarchitecture and Simplified Boundary Conditions Limit the Accuracy of Quantitative  
412 Computed Tomography-Based Finite Element Models of Vertebral Failure. *J Biomech Eng* 140,  
413 1–11. <https://doi.org/10.1115/1.4038609>

414 Jackman, T.M., DelMonaco, A.M., Morgan, E.F., 2016. Accuracy of finite element analyses of CT scans  
415 in predictions of vertebral failure patterns under axial compression and anterior flexion. *J*  
416 *Biomech* 49, 267–275. <https://doi.org/10.1016/j.jbiomech.2015.12.004>

417 Knowles, N.K., G. Langohr, G.D., Faiegghi, M., Nelson, A., Ferreira, L.M., 2019. Development of a  
418 validated glenoid trabecular density-modulus relationship. *J Mech Behav Biomed Mater* 90, 140–  
419 145. <https://doi.org/10.1016/j.jmbbm.2018.10.013>

420 Lawless, I.M., Ding, B., Cazzolato, B.S., Costi, J.J., 2014. Adaptive velocity-based six degree of freedom  
421 load control for real-time unconstrained biomechanical testing. *J Biomech* 47, 3241–3247.  
422 <https://doi.org/10.1016/j.jbiomech.2014.06.023>

423 Lin, Z.X., Xu, Z.-H., An, Y.H., Li, X., 2016. In situ observation of fracture behavior of canine cortical  
424 bone under bending. *Mater. Sci. Eng. C* 62, 361–367. <https://doi.org/10.1016/j.msec.2016.01.061>

425 Liu, L., Morgan, E.F., 2007. Accuracy and precision of digital volume correlation in quantifying  
426 displacements and strains in trabecular bone. *J Biomech* 40, 3516–3520.  
427 <https://doi.org/10.1016/j.jbiomech.2007.04.019>

428 Mao, Q., Su, K., Zhou, Y., Hossaini-Zadeh, M., Lewis, G.S., Du, J., 2019. Voxel-based micro-finite  
429 element analysis of dental implants in a human cadaveric mandible: Tissue modulus assignment  
430 and sensitivity analyses. *J Mech Behav Biomed Mater* 94, 229–237.  
431 <https://doi.org/10.1016/j.jmbbm.2019.03.008>

432 Martelli, S., Perilli, E., 2018. Time-elapsd synchrotron-light microstructural imaging of femoral neck  
433 fracture. *J Mech Behav Biomed Mater* 84, 265–272. <https://doi.org/10.1016/j.jmbbm.2018.05.016>

434 Nazarian, A., Müller, R., 2004. Time-lapsed microstructural imaging of bone failure behavior. *J Biomech*  
435 37, 55–65. [https://doi.org/10.1016/S0021-9290\(03\)00254-9](https://doi.org/10.1016/S0021-9290(03)00254-9)

436 Oliviero, S., Giorgi, M., Dall'Ara, E., 2018. Validation of finite element models of the mouse tibia using  
437 digital volume correlation. *J Mech Behav Biomed Mater* 86, 172–184.  
438 <https://doi.org/10.1016/j.jmbbm.2018.06.022>

439 Palanca, M., Bodey, A.J., Giorgi, M., Viceconti, M., Lacroix, D., Cristofolini, L., Dall'Ara, E., 2017.  
440 Local displacement and strain uncertainties in different bone types by digital volume correlation  
441 of synchrotron microtomograms. *J Biomech* 58, 27–36.  
442 <https://doi.org/10.1016/j.jbiomech.2017.04.007>

443 Palanca, M., Cristofolini, L., Dall'Ara, E., Curto, M., Innocente, F., Danesi, V., Tozzi, G., 2016. Digital  
444 volume correlation can be used to estimate local strains in natural and augmented vertebrae: An  
445 organ-level study. *J Biomech* 49, 3882–3890. <https://doi.org/10.1016/j.jbiomech.2016.10.018>

446 Rice, J., Cowin, S., Bowman, J., 1988. On the dependence of the elasticity and strength of cancellous  
447 bone on apparent density. *J Biomech* 21, 155–168. [https://doi.org/10.1016/0021-9290\(88\)90008-](https://doi.org/10.1016/0021-9290(88)90008-5)  
448 5

449 Roberts, B.C., Perilli, E., Reynolds, K.J., 2014. Application of the digital volume correlation technique  
450 for the measurement of displacement and strain fields in bone: a literature review. *Journal of*  
451 *biomechanics* 47, 923–934. <https://doi.org/10.1016/j.jbiomech.2014.01.001>

452 Schaffler, M.B., Burr, D.B., 1988. Stiffness of compact bone: effects of porosity and density. *J Biomech*  
453 21, 13–16. [https://doi.org/10.1016/0021-9290\(88\)90186-8](https://doi.org/10.1016/0021-9290(88)90186-8)

454 Schneider, C.A., Rasband, W.S., Eliceiri, K.W., 2012. NIH Image to ImageJ: 25 years of image analysis.  
455 *Nat Methods* 9, 671.

456 Sukjamsri, C., Geraldles, D.M., Gregory, T., Ahmed, F., Hollis, D., Schenk, S., Amis, A., Emery, R.,  
457 Hansen, U., 2015. Digital volume correlation and micro-CT: An in-vitro technique for measuring  
458 full-field interface micromotion around polyethylene implants. *J Biomech* 48, 3447–3454.  
459 <https://doi.org/10.1016/j.jbiomech.2015.05.024>

460 Terrier, A., Büchler, P., Farron, A., 2005. Bone–cement interface of the glenoid component: stress  
461 analysis for varying cement thickness. *Clin Biomech* 20, 710–717.  
462 <https://doi.org/10.1016/j.clinbiomech.2005.03.010>

463 Walker, M.R., Dickey, J.P., 2007. New methodology for multi-dimensional spinal joint testing with a  
464 parallel robot. *Med Biol Eng Comput* 45, 297–304. <https://doi.org/10.1007/s11517-006-0158-6>

465 Zael, R., Yeni, Y.N., Bay, B.K., Dong, X.N., Fyhrie, D.P., 2005. Comparison of the Linear Finite  
466 Element Prediction of Deformation and Strain of Human Cancellous Bone to 3D Digital Volume  
467 Correlation Measurements. *J Biomech Eng* 128, 1–6. <https://doi.org/10.1115/1.2146001>

468 Zheng, M., Zou, Z., Bartolo, P., jorge D. silva, Peach, C., Ren, L., 2017. Finite element models of the  
469 human shoulder complex: a review of their clinical implications and modelling techniques: Finite

470 Element Models of Human Shoulder Complex. *Int J Numer Method Biomed Eng.* 33, e02777.  
471 <https://doi.org/10.1002/cnm.2777>  
472 Zhou, Y., Lamberty, M.A.H., Lewis, G.S., Armstrong, A.D., Du, J., 2018. 3D Full-Field Mechanical  
473 Measurement of a Shoulder Bone Under Implant Loading, in: *TMS Annual Meeting &*  
474 *Exhibition*. Springer, pp. 287–293. [https://doi.org/10.1007/978-3-319-72526-0\\_26](https://doi.org/10.1007/978-3-319-72526-0_26)  
475